# How fluid-mediated rock transformations can mimic hydro-fracturing patterns in hydrothermal dolomite

Stephen Centrella, Nicolas Beaudoin, Daniel Koehn, Geoffrey Motte, Guilhem Hoareau, Jean Paul Callot

▶ To cite this version:

Stephen Centrella, Nicolas Beaudoin, Daniel Koehn, Geoffrey Motte, Guilhem Hoareau, et al.. How fluid-mediated rock transformations can mimic hydro-fracturing patterns in hydrothermal dolomite. Marine and Petroleum Geology, 2022, 140, pp.105657. 10.1016/j.marpetgeo.2022.105657 . hal-04273379

HAL Id: hal-04273379
https://hal.science/hal-04273379v1

Submitted on 7 Nov 2023

# How fluid-mediated rock transformations can mimic hydro-fracturing patterns in hydrothermal dolomite

Stephen Centrella (1), Nicolas E. Beaudoin (1), Daniel Koehn (2), Geoffrey Motte (1, 3), Guilhem Hoareau (1), Jean Paul Callot (1).

1 Universite de Pau et des Pays de l'Adour, E2S UPPA, LFCR, CNRS, TotalEnergies, Pau, France

2 GeoZentrum Nordbayern, University Erlangen-Nuremberg, Schlossgarten 5, 91054, Erlangen, Germany

3 GEOSEDIA, 64000, Pau, France

## Abstract

Numerous studies of hydrothermal dolomite bodies describe brecciated rocks characterized by dark angular fragments of dolomicrite bounded together by saddle dolomite crystals forming veins. Often associated with ore deposits, these hydrothermal dolomite breccia (HDB) patterns are usually interpreted as related to hydro-fracturing and so are considered as univocal markers of fluid overpressure. In this contribution we challenge this interpretation by investigating the textural and crystallographic patterns of a HDB related to Mesozoic hyper-extension located in the Northern Pyrenees (France). The following observations lead us to propose that this HDB results from texturally controlled, hydrothermal fluid-initiated recrystallization of the initial sedimentary breccia by grain boundary migration: (1) the occurrence of rough contacts between the dolomite crystals and an initial dolomitized sedimentary breccia structure; (2) the crystallographic pattern of the hydrothermal dolomite; (3) the different grain size distribution in HDB texture and initial breccia structure; (4) the spatial distribution of oxide particles. Our alternate interpretation was further tested by 2D numerical simulations of the replacement process using the 'ELLE' modelling toolbox. Simulations confirm that advection of hot fluids along porous zones can locally trigger recrystallization by grain boundary migration, a replacement of the initial breccia texture and a preservation of larger, less permeable and cold fragments. We propose key features in textural evidence to assess whether HDB texture is pinpointing towards episodes of fluid overpressure and fracturing in carbonates, or if it rather is related to fluid-mediated rock recrystallization.

Keywords: Hydrothermal; Dolomite; Breccia; Modelling; Recrystallization

## 1 Introduction

Fluid overpressure (i.e. supra-hydrostatic pressure) in sedimentary rocks is a complex and important phenomenon (Cobbold and Rodrigues, 2007; Koehn et al., 2020) as it often leads to fracture development that strongly alters reservoir quality (Roure et al., 2010), breaks seals (Bons et al., 2012; Cornet et al., 2003), induces seismicity (Baisch, 2020; Sibson, 2012; Zoback and Townend, 2001), triggers mineral precipitation that can trap carbon (Vass et al., 2014), and controls fluid migration (Bjørlykke and Middleton, 2003). Current monitoring of the pressure state in sedimentary rocks shows that many exploited basins fall into a supra-hydrostatic regime (Beaudoin et al., 2014). Yet, reconstructing quantitatively the past fluid-pressure regime is challenging and relies on proxies such as deformation features (Amrouch et al., 2011; Gudmundsson, 2001; Passelègue et al., 2014), presence of organic matter (Wang et al., 2020), or microthermometry of coeval aqueous and hydrocarbon-bearing fluid inclusions (Pironon, 2004). A qualitative proxy to pinpoint that fluid overpressure locally overcame lithostatic stress is the observation of specific breccia patterns in hydrothermal dolomite, the so-called hydrothermal dolomite breccia (HDB). Generally, HDB are thought to be dolomite-cemented rocks that develop when fluids flow through a system where cracks were generated by fluid overpressure (Davies and Smith, 2006). HDB display a characteristic pattern made up of black angular fragments (the clasts) surrounded by a cement formed by the direct precipitation of euhedral and saddle dolomite crystals (Fig. 1). HDB are often associated with an abnormally high geothermal gradient (much higher than the average 30°C/km), sometimes bound to ore deposits or hydrocarbons, and are documented worldwide: Hungary (Garaguly et al., 2018), Spain (Iriarte et al., 2012; López-Horgue et al., 2010), French Alps (Barale et al., 2013; Malaroda, 1999), French Pyrenees (Incerpi et al., 2020; Salardon et al., 2017), Italy (Iannace et al., 2012), United Kingdom (Hendry et al., 2015), Canada (Haeri-Ardakani et al., 2013; Mattes and Mountjoy, 1980), Lebanon (Nader et al., 2004), Oman (Beckert et al., 2015), South China (Chen et al., 2004), NW China (Guo et al., 2016; Wang et al., 2019).

The Jurassic dolostones of the Mano Formation in the Mail Arrouy shows HDB patterns. It is located in the *Chaînons Béarnais* (Northwest Pyrenees, France, Fig. 2), developed as a response to Mesozoic hyper-extension of the crust and to related salt tectonic activity. Diagenetic studies in the area relate saddle dolomite in the HDB pattern to regional-scale hydrothermal fluid flow coeval to the extension of the crust, with absolute age corresponding to Albian time (111-106 Ma) (Motte et al., 2021; Salardon et al., 2017). Based on the geometry of clasts in the HDB patterns, structures in the Mail Arrouy resulted from brittle deformation related to fluid overpressure ("Fluid-assisted brecciation"), a chemical reaction, a decompression or a phreatic explosion ("volume expansion") (Jébrak, 1997). Petrological evidences across the contact between the HDB and a preexisting dolomitized sedimentary breccia, that shows no sign of hydro-fracturing, suggests another governing mechanism. By using surface analysis on polished slabs and textural analyses (scanning electron microscopy (SEM) and electron backscattered diffraction (EBSD)), we reconstruct the genetic link between the original breccia and the HDB pattern, proving that the cement is likely to represent a recrystallization of pre-existing dolomite. Numerical simulations validate the role of hydrothermal fluids in the origin of observed textures, allowing to propose an alternative mechanism of development for the HDB pattern in the Mano formation, which does not summon either hydro-fracturing nor volume expansion, but rather temperature-triggered grain boundary migration**.**

## 2 Geological setting

### 2.1 Mail Arrouy Anticline

The Mail Arrouy Anticline belongs to the *Chaînons Béarnais*, a series of E-W striking anticlines located in the Northern Pyrenean zone (France, Fig. 2). At the Mail Arrouy Anticline a sedimentary stack comprising Triassic evaporites, the marine successions of the Jurassic and the Cretaceous marine carbonate rocks crop out (Lenoble, 1992). Deposition of Jurassic platform carbonates was followed by widespread marine regression and sediment emersion from the end of the Tithonian to the Neocomian (Grimaldi, 1988). From Barremian to Aptian, a marine transgression flooded the partially eroded Jurassic carbonate succession rocks. As the same time, the crust was stretched, thinned, leading to high geothermal gradients due to mantle exhumation (Clerc et al., 2015; Tugend et al., 2015; Vacherat et al., 2014). From the Campanian onwards, the convergence between the European and the Iberian plates resulted in the Pyrenean orogeny (Mouthereau et al., 2014). The geometry of the fold results both from extension-related down-building and gravitational gliding above evaporites, and from folding during the subsequent convergence-related shortening phase (Izquierdo-Llavall et al., 2020; Labaume and Teixell, 2020).

### 2.2 The hydrothermal dolomite breccia of the Mano formation

The Mano Formation is a Tithonian dolostone related to a peritidal carbonate platform environment. In this formation, two type of breccia are in contact with each other (Fig. 3): (1) a hydrothermal breccia dolostone characterized by monogenic angular clasts with a dolomite cement with planar and saddle texture, corresponding to a cemented rubble float-breccia morphology (Morrow, 1982) (Fig. 3a, b, d); (2) a second breccia that exhibits monogenic angular clasts with dolomitized mud in between, corresponding to a particulate rubble pack-breccia morphology (Morrow, 1982) (Fig. 3d, f, g h). The latter was fully dolomitized during marine transgression (Neocomian-Barremian) (Grimaldi, 1988; Motte et al., 2021). For the sake of clarity, we will hereinafter refer to the large white dolomite crystals in between the clast of the HDB as “cement”, while the dolomitized mud in the original breccia is referred to as “matrix”.

According to Motte et al. (2021), the minimum precipitation temperature of the planar and saddle dolomite in the HDB ranges progressively from 196 °C in the vicinity of the clast to 320 °C in the centre of the cement (Fig. 4). A mostly crustal or sedimentary origin for hydrothermal fluid was proposed in accordance with rare earth element patterns (Motte et al., 2021) (Figure 3d).

# 3 Methods

## 3.1 Surface analyses

Eleven (11) samples were collected on meter-scale outcrops (Fig. 3b) from which thin-sections of 45 x 60 mm (5) and polished slabs (4) were made in both the sedimentary breccia and the hydrothermal dolomite breccia. Among those, one 0.5 x 0.3 m block was selected to investigate the textural properties of both breccias (Fig. 5). This sample shows the HDB pattern quite well and displays the contact between the two types of breccias (HDB and sedimentary). Surface measurements and clast size distribution were undertaken in both the HDB pattern and in the original breccia. High-resolution scans (pixel size of 22 microns) were processed with Dragonfly v.4.0, a proprietary image analysis software normally used for 3D reconstruction. The image noise was reduced using a median filter (Kernel size 3). Clasts were selected using grey value thresholding in 8-bits. When clasts are crossed by veins the latter were suppressed manually. Surface areas were computed for each segmented clast by a pixel count over areas of a constant size (24 985.6 x 23 472.80 µm). The size distribution of the clast population was modelled in both HDB and original breccia. For the specific case of porosity, percentage of pixels was estimated based on a 2D analyses of BSE images (Fig. 6). Porosity was segmented using grey value thresholding applied on 8-bits images. As the contrast is very strong between the porosity and dolomite greyscale, we consider the error on the phase selection to be negligible.

### 3.2 Electron backscattered diffraction (EBSD)

EBSD analysis was carried out at the Centre de Micro-Caractérisation Raimond Castaing at Toulouse, using a SEM JEOL JSM-7100TTLS LV. EBSD data were acquired using an Oxford Instruments Aztec 3.4 EBSD and EDS system using an accelerating voltage of 20 keV and a beam size of 5 µm. Post-processing of EBSD data was done using the HKL Oxford Instruments Channel 5 v.5.12.72.0 software. A noise correction was applied based on a replacement of single pixels that are different (by some misorientation) from 8-7 and 6 nearest neighbours was applied. A Kuwahara filter was used to erase the effect of polishing with 3 x 3 pixels and a 5° angle. This method aims to get crystallographic information across different interfaces to see the relationship between the three dolomites.

### 3.3 Numerical Modelling

We used a numerical hydro-dynamic reactive transport model to simulate the microstructural development (Module “Latte” within modelling environment “Elle” (Bons et al., 2008b; Koehn et al., 2021; Koehn et al., 2020; Piazolo et al., 2019)) to validate the process that could account for the development of HDB pattern while explaining the contrast in clast size distribution and the contacts between cement and matrix phases. We used 2.2 x 2.2 mm extract of EBSD maps of representative area of unreacted original breccia, along with porosity estimated from BSE images, as the initial mesh for the simulations (Fig. 5).

In the simulation, a granular domain is infiltrated by a hydrothermal compressible fluid. The temperature evolution is a function of the advection-diffusion equation for heat transport, as a function of the hydro-dynamic fluid infiltration and the Darcy velocity. The breccia is assumed to be a granular media with a background porosity and with grain boundaries that have a higher permeability than the clasts assuming laminar channel flow. The replacement reaction is a function of the temperature and is modelled using an Arrhenius equation. The model is a two-dimensional representation of the initial sedimentary breccia with a triangular mesh of cells and clusters of cells representing larger grains. The fluid properties are calculated on a second square grid with cells that are twice as wide as the diameter of the solid cells. Boundary conditions are high fluid pressure and temperature at all four boundaries of the model, so that the fluid is infiltrating from all sides. The model cycles through an initial calculation of the fluid pressure evolution using a compressible fluid and calculating how this fluid fills the model domain. This step is followed by the calculation of the temperature advection as a function of the Darcy velocity from the fluid evolution. As a second step, temperature diffusion is calculated, which is followed by a final calculation of the replacement reaction as a function of the local temperature. The loop is repeated each time step where the time is non-linear and calculated before each loop to optimize speed while retaining stability of the solvers.

The breccia is represented by a granular aggregate with a porosity defined by the solid fraction of the network within a fluid cell. Grain boundaries in the aggregate are thought to be channels where fluid flow is in the viscous regime with a linear relationship between the average flow velocity in the channel and the pressure gradient in the fluid. For a simple Poiseuille flow in the channel the permeability is $a^2/12$ with $a$ being the width (or aperture, $10^{-7}$m) of the grain boundary (Flekkøy et al., 2002). This permeability is tensorial in nature but can be simplified for modelling purposes by averaging over different spatial directions (Flekkøy et al., 2002) , and by adding a Carman-Kozeny relation for the rest of the cell, assuming it can be represented by a porous media (Carman, 1937; Ghani et al., 2013) according to

$$K(\phi_{x,y}) = \frac{r^2(\phi_{x,y})^3}{45(1-\phi_{x,y})^2} + \frac{a^3}{24\, l_0} \qquad (eq\ 1)$$

The first term on the right-hand side is representing the background permeability and the second term is representing the grain boundary permeability, where r is a fixed grain size ($10^{-5}$ m), $\phi_{x,y}$ the local porosity (0.03-0.1) and $l_0$ the grid size ($10^{-5}$ m).

In a first step, the fluid pressure evolution is calculated as a function of variations in porosity and permeability, as well as the pressure gradient using the following equation (Koehn et al., 2020).

$$\phi\beta\left[\frac{\partial P}{\partial t}\right] = \nabla\cdot\left[(1+\beta P)\frac{K}{\mu}\nabla \mathrm{P}\right] \qquad (eq\ 2)$$

with $\phi$ porosity (0.03-0.1), $\beta$ fluid compressibility (4.5 x $10^{-10}$ $m^2/N$), $P$ fluid over-pressure (0-10MPa), $K$ permeability ($m^2$ from eq.1), $\mu$ fluid viscosity ($10^{-3}$ Pa/s). The fluid velocity $\vec{v}$ (m/s) from the Darcy fluid $\phi\vec{v}$ of the infiltrating fluid for temperature advection is calculated according to

$$\vec{v} = -\frac{\frac{K}{\mu}\nabla P}{\phi} \qquad (eq\ \ 3)$$

The effects of temperature advection and diffusion are separated and added after each time step according to

$$T^{t} = T^{t-1} + \delta T_{adv}^{t} + \delta T_{diff}^{t} \qquad (eq\ 4)$$

solving the heat equation

$$\frac{\partial T}{\partial t} + \vec{v}\,\nabla T - D\Delta T = f \qquad (eq\ 5)$$

with $D$ the thermal diffusion coefficient (1.5 $10^{-6}$ $m^2.s^{-1}$). Advection is solved explicitly and diffusion implicitly with non-linear time steps defined by the fluid pressure equation and internal time stepping within the advection equation for stability. The advection is solved using the Lax-Wendroff scheme (Lax and Wendroff, 1960) with

$$\delta T_{adv}^{t} = -dt\,\vec{v}\,\nabla T^{t-1} \qquad (eq\ 6)$$

as a function of the local fluid velocity. Temperature diffusion is solved using an implicit ADI algorithm (Bons et al., 2008a) with

$$\delta T_{diff}^{t} = dt\,\Delta\left(T^{t-1} + \delta T_{diff}^{t}\right) \qquad (eq\ 7)$$

As a last step the replacement reaction is a function of the local temperature according to

$$k = A \cdot exp^{-\frac{E_A}{RT}} \qquad (eq\ 8)$$

with k the reaction rate (m/s), A a prefactor (m/s), $E_a$ activation energy (J $mol^{-1}$), R the universal gas constant (8.3145 J $mol^{-1}K^{-1}$) and T the temperature (K).

# 4 Results

## 4.1 Surface analysis

The contact of the clasts with the matrix is smooth with sharp without a significant roughness (Fig. 3f, g, h) whereas the contact between the cement and the clasts, and between the cement and the matrix, is rough on the sub-millimetre scale (black arrows in Fig. 4). Iron oxides are mainly located at the edge of the clasts in the original breccia (Fig. 3d-h), whereas in the HDB they are mainly present at the tip of saddle dolomite crystals (Fig. 3d and e). 1-3 mm large quartz are located only in the centre of the veins (Fig. 3d and e). The sample that was used for modelling grain size distribution from phase analysis is presented in Figure 5. The analysed HDB section of the sample is composed of 51 clasts with a median surface area of around 1.67 mm² and a minimum fragment surface of 0.17 mm² (Fig. 5b and c). The second section representing the clasts and brown matrix has 1777 clasts with a median surface area of 0.009 mm² and a minimum fragment surface of 0.003 mm² (Fig. 5 d and e). The third section contains matrix, cement and clasts and show that smaller clasts are located in the matrix whereas they are not present in the cement (Fig. 5f and g).

## 4.2 EBSD-Analysis

Two EBSD maps were constructed to study the textural relationship between clasts, matrix and cement.

The first map is positioned in an area where the original breccia is dominant with matrix and clasts (Fig. 7; location in Fig. 3e, 180° reversed), returning a large variation in clasts size (Fig. 7a and b). This area is composed of calcite, dolomite, quartz and iron oxides (Fig. 7c). The clasts are composed of dolomite crystals as small as 50 µm in diameter (Fig. 7d) with a strong crystallographic preferred orientation (CPO) along the c-axis (Fig. 7e zones 3 and 4). The matrix comprises of dolomite crystals with heterogeneous size (~50 to 150 µm) characterized by a complete preservation of the shape of constitutive grains such as ooids, and no CPO (Fig. 7e zones 1 and 2). The cement comprises of dolomite crystals of which size ranges between 50 to 350 µm (Fig. 7d).

The second map is focused on the cement (Fig. 8; location in Fig. 3c). The phase-map shows the presence of dolomite, calcite, quartz and locally some iron oxide (Fig. 8a). Small quartz crystals are present in the clasts. Calcite is located at the inner rim of saddle dolomite crystals, associated with iron oxides. The clasts are composed of small crystals less than 50 µm in diameter whereas in the cement the crystal size increases from ~50 to ~1300 µm toward the quartz (Fig. 8b). Cement dolomite is characterized by low-angle boundaries that are shared between different crystals (< 2°, Fig. 8c). The GROD (grain reference orientation deviation) of these crystals presents a gradual variation from 0 to 20°. perpendicular to the clast interface (Fig. 8d).

## 4.3 Numerical Modelling

### 4.3.1 Scaling the simulation

The model simulates the constant infiltration of a hot fluid at a given temperature in a colder host rock, which then heat the dolomite grains and triggers a recrystallization by grain boundary migration (sensu Kelka et al., 2015). The simulation accounts for the temperature of the fluid and host-rock using values estimated from microthermometric studies on fluid inclusions (Motte et al., 2021). The incoming fluid is considered to be 300°C hot, while the dolomite matrix and clasts initially have a temperature of 200°C (Fig. 4e). The simulation takes into accounts that half the clasts documented in the HDB have an area smaller than 1.67 mm² (i.e. the median value for the clast size distribution), which corresponds to an 1D clast size of 1.29 mm (assuming square shapes). The smallest clasts are around 0.17 mm², corresponding to a 0.40 mm clast size in 1D (Fig. 5). To account for the variation in the clast sizes over 1 order of magnitude, the model setup uses a 400 x 400 pixel grid of the original dolomitized breccia structure allowing a range of clast size from x100 µm to 2.2 mm (location in Fig. 7b), so that the smallest possible clast size corresponds to the grid size of 5.5 µm in 1D. Grain sizes were defined by the grain boundary angle obtained with EBSD data according to orientation mismatch (see Fig. A.1 for processing details). The model box corresponds to a square of 2.2x2.2 mm size. Using 2D analyses of BSE images (Fig. 8), the porosity in the matrix is about 6 to 10 vol.% and ca. 4 vol.% in the clasts. In the model, the background porosity within grains in the matrix and clasts is 3-4 vol.%.

Experimental data on thermal diffusion coefficient of dolomite ranges from 1.471. $10^{-6}$ $m^2.s^{-1}$ to $1.573.10^{-6}$ $m^2.s^{-1}$ (Xiong et al., 2020). Due to the difference in mineral composition, grain size or porosity, thermal conductivity can change in the same lithology (Xiong et al., 2020). We use 1.5 $10^{-6}$ $m^2.s^{-1}$ as basic thermal diffusion coefficient in grain boundaries in the simulation and adjust intra-grain diffusion according to variations in porosity. In the case of dolomite, (Thomas et al., 1973) have shown that thermal conductivity of water saturated dolomite samples changes from 5.5 to 4.2 W $m^{-1}$ $C^{-1}$ at 40.5°C, between coarse (~ 200 µm) and fine grain sample (< 100 µm) due to the increase of solid-solid contacts.

#### 4.3.2 Outcomes of simulations

We undertook a series of 4 simulations assuming that (1) the heat is provided only by constant hydrothermal fluid flux into the system from all sides and (2) that temperature difference drives the recrystallization process (Fig. 9). Since we consider that heat is brought in only by the fluid flux, one can consider the thermal Péclet number to be similar to the fluid dynamics Péclet number (i.e. ratio between fluid advection and fluid diffusion). Hence, a large Péclet number represents an advection dominated system and a low Péclet number a diffusion dominated system. Since the thermal diffusivity is constant, changes in fluid velocity and thus advection drive changes in the Péclet number. Each simulation step represents a time that scales for the different runs between 0.4 seconds to 5 hours/model step (Fig. 9). The developing replacement front is faster when the Péclet number is large (10 to 100) and advection is dominating. Under these circumstances the fluid infiltrates along the grain boundaries, which are much more dominant in the matrix region compared to the large clasts.

As a result, with a Péclet number of 100 the large (>1 mm) and even the intermediate (0.5 – 1 mm) clasts are not replaced. The reaction front itself is very rough with local fingering. With a Péclet number of 10, the front becomes less rough, replaces all the small matrix grains and leaves out the larger clasts. At a Péclet number of 1 diffusion and advection are equal in rates and the front becomes smooth. Large clasts are replaced at a slower rate driven by diffusion into the clasts but they are slowly replaced as well. At a Péclet number of 0.1 diffusion takes over and replaces the whole aggregate with a very smooth but wide reaction front.

To compare these results with the natural hydrothermal breccia (Fig. 3a and b), it is important to look at the last column on the right-hand side in the simulations that represents the distribution of 90% to 100% replacement of the original dolomite at the last step of the simulation (150000). The similarity of the roughness of the front replacement visible in natural clasts and clasts in the model agrees the most with a Péclet number close to 10. This leads to the complete replacement of ~17 % of the original volume (0.73 $mm^2$) within a few minutes for the considered area.

# 5 Discussion

## 5.1 Fluid-mediated, temperature controlled dynamic recrystallisation can form hydrothermal dolomite breccia

The investigation of the reaction front between the HDB and the original sedimentary breccia structure allows us to propose an alternative model of the formation of HDB, that does not require high fluid overpressure that fractures the rock. Our new hypothesis and model, detailed below, also unravels the fluid dynamics and controlling factors of the fluid infiltration into the porous media (Fig. 10).

### 5.1.1 Dolomitization of the initial sedimentary breccia by coupled dissolution-precipitation

We propose the following history: a first fluid dolomitized the original sedimentary breccia (Grimaldi, 1988), concentrating oxides at clast's surfaces during recrystallization. This process is known from the so called Zener pinning, where two processes take place, the grain boundaries are pinned by impurities or the impurities are moved by the boundaries and are included into them (Kelka, 2017; Kelka et al., 2015). Typically, a combination of both processes takes place in rocks, where large and high concentration of impurities favours boundary pinning whereas fast grain boundaries, small and low concentration of impurities favours clearing grains of impurities and collecting them in the boundaries. The replacement of calcite by dolomite has preserved the original shape of a large number of sedimentary features in the breccia, such as ooids in the matrix and the largest clasts, with some calcite still being visible (Fig. 3 and 7). All clasts present the same crystallographic preferred orientation (CPO) along the c-axis meaning that the crystallization was under the same stress regime (Fig. 7e). During this first dolomitization event, the CPO might have been preserved by a dissolution-precipitation mechanism. This preservation is known to take place in experiments where the crystallographic orientation of the parent mineral can be transferred to the new mineral (O'Neil, 1977; O'Neil and Taylor, 1967; Putnis and Austrheim, 2013; Yanagisawa et al., 1999). This may be realistic, because recent experimental work on dolomitization and on natural examples have shown that dolomitization occurs with a dissolution-precipitation mechanisms (Centrella et al., 2020; Jonas et al., 2017; Jonas et al., 2015). While the studied rocks in the basin were emersed, karst was formed where an original dolomite layer was broken and mixed with muddy sediment. This leads to the initial background texture where HDB will then develop (Fig. 10a).

### 5.1.2 Formation of hydrothermal dolomite breccia by grain boundary migration

Since there are more grain boundaries in the matrix than in the clasts (Fig. 9), hydrothermal fluid infiltration into the matrix is faster (Fig. 9 and Fig. 10b). As fluid locally creates a strong temperature gradient (infiltrating with a temperature of ~300°C while the host temperature is ~200°C), it would triggers recrystallization of the matrix by grain boundary migration that cleanses oxides that migrate to the tip of the saddle dolomite in accordance with Zener pinning (Kelka, 2017; Kelka et al., 2015) (Fig. 10c). Further on, low-angle boundaries (Fig. 8c) can form directly during the mineral formation and bear similarities to microstructures formed by crystal-plastic deformation, for example in high strain zones (Harlov and Austrheim, 2013). The high roughness of the cement-matrix and clast-cement contacts supports this advection-dominated reaction (Koehn et al., 2021; Szymczak and Ladd, 2014, 2013, 2009). The fact that the recrystallization does not affect the whole initial breccia, and that clasts above a certain size are preserved, suggests that the thermal source (i.e. the hydrothermal fluid at 300°C) was not maintained long enough to recrystallize the whole domain. The flow of hydrothermal fluid at 300°C must not have been sustained long enough to lead to a complete recrystallization, and points towards more episodic hydrothermal fluid flow in the area. The fact one can observe corona structure of the dolomite cement around the clasts, that corresponds to smaller dolomite grains, supports that the recrystallization dissipated thermal energy from the matrix towards the clast. In other words, the corona around the clasts would be small grains that show only the beginning of grain boundary migration in the area (Fig. 7). The quartz that is systematically documented in the centre of coarse dolomite cement has been interpreted as related to the posterior contraction event (Upper Cretaceous) based on geochemical characterization (Motte et al., 2021). Hence it seems unrelated to the diagenetic history of the breccia of which the small crystal (the coronas) has been dated by U-Pb absolute dating method the Albian time (111 – 101 Ma) (Motte et al., 2021). Textural observation suggest the quartz fills up intercrystalline porosity, suggesting either an unlikely dissolution localized at the centre of the dolomite cement, or that the grain boundary migration left voids in the centre of the band of cement, which is observed in other systems where grain boundary migration occurs (e.g. zebra dolomite, Kelka et al., 2015).

## 5.2 Timescale of hydrothermal dolomite breccia development

The simulations indicate that the recrystallization transforming the sedimentary breccia to an HDB pattern was induced by infiltrating fluids with a high Péclet number of 10, indicating that advection was dominating, and diffusion only played a minor role (Fig. 9). In terms of timescales the advective transport will have taken part relatively fast along grain boundaries, with a Darcy velocity between $10^{-7}$ to $10^{-10}$ m/sec. According to the Péclet number, the model predicts a replacement of 0.42 $mm^2$ to 0.73 $mm^2$ in a time frame ranging from 5 seconds to 3 minutes. The small grains (< 200 µm) with a high surface area will be able to replace fast because they are directly in contact with the high temperature fluid and diffusion into the crystal is fast. In contrast, larger clasts (> 1 mm) will need diffusion to be active for longer or a longer presence of hot fluid for heat to progress into the clast and for the reaction to be driven. In addition, the hot domains in the grain boundaries are very small so that the heat reduces very fast during diffusion and needs further advection to take place. Finally, according to the rate law used, the reaction front can propagate by about 80 µm per hour in a single grain. This implies that if the grains are smaller and in contact with the fluid, they can replace faster due to a higher reactive surface. Diffusion can equalize temperatures very fast on the small scale. However, the grain boundaries that contain the high temperature fluid are very small and the temperature will dissipate very fast within the sample, almost not heating it up unless more hot fluid is advected. Larger grains of 2 mm in size can be heated within 2 seconds but need then about 10 seconds to be replaced. This ratio switches at the centimetre scale, where diffusion becomes slower than the reaction and rate limiting. To sum up, at least in the case studied here, formation of HDB is advection controlled and develops sub-instantaneously at the geological timescale. For the bigger grains (> 200 µm), the transition from reacted to unreacted clasts represents the diffusion length scale that limits the reaction in the range of seconds to hours. This hydrothermal event of HDB formation can thus be explained by a single event under temperature gradient. This extremely fast reaction has fundamental impact on our understanding on fluid flow in porous media.

### 5.3 Do we have to question other HDB?

In Figure 1, we listed HDB documented across the world that in spite of various geological context and fluid nature, are all formed with abnormally high geothermal gradients. In all these cases, we can define two key textural features based on the study of the HDB pattern from the Mail Arrouy, that will allow to diagnose whether the HDB is related to hydrofracturing or to fluid-mediated recrystallization. The first thing to look for is the contact roughness between clast and cement visible on polished sample. If it is rough (Fig. 1 e, f, g and Fig. 4), then it is important to look at the cement structure with EBSD to see if there is a general increase of crystal size toward the clast with sub-grains boundaries shared between crystals (Fig. 8). Second, the distribution of clast size (all above a certain size) and localization of oxides at clast boundaries and/or at the tip of the saddle crystals of the cement both hint towards recrystallization by grain boundary migrations. If one or all of these observations are present, there is a high probability that the hydrothermal dolomite breccia resulted from fluid infiltration followed by recrystallization rather than by hydro-fracturing. The texture naturally implies the presence of a pre-existing rock matrix, may it be a fractured zone, small grains or the matrix of a pre-existing breccia before the hydrothermal fluid infiltration even if there is no trace of the matrix anymore. These observations challenge the way HDB used to be interpreted and the geodynamic reconstruction associated: high fluid overpressure that leads to hydrofractures does not have to be the responsible mechanism for their formation but rather reactive fluid-mediated replacement. This does not mean that high fluid pressures cannot be present, and indeed pressure gradients are certainly needed for the advective process to take place. HDB may still fracture and react at the same time, but they are not a direct indicator of fluid overpressure above lithostatic pressure. What is even more clear is that the unreacted dark pieces are not representing the full host rock that fractured and the veins are not filled fractures. Rather the veins are replaced zones that are easier infiltrated and react faster, whereas the large "breccia" pieces are uncreated remnants. This approach may be transferred to other systems, and one might question the role of fluid overpressure in similar patterns encountered in hydrothermal calcite breccia (Peacock et al., 2019) and in serpentine rocks (Bach et al., 2006; Lafay et al., 2017).

## 6 Conclusions

Morphological, textural and numerical modelling data reported here suggest that the HDB from the Mail Arrouy resulted from a fluid-mediated reaction triggering grain boundary migration from initial sedimentary breccia and highlight the importance of pre-existing sedimentological heterogeneities in fluid flow. A range of arguments, including subgrain distribution, contact roughness, clast size distribution variation between the original breccia and the HDB, and the oxide repartitioning at the tips of the cement all support the hypothesis that migration of grain boundaries rather than fracturing is the actual mechanism forming these rocks. Hydrothermal fluids will locally increase the temperature where it infiltrates, triggering a grain boundary migration that will (1) replace matrix and clasts up to a certain size due to a transition from reaction to diffusion-controlled time scales, and (2) develop rough contacts where the reaction stops because of thermal dissipation likely related to a stop in the hydrothermal fluid flow. Because the simulation reproduces patterns visible on the natural HDB it allows a scaling of this process ranging from seconds to days according to the surface and advective speed considered. We conclude that neither tectonic hydro-fracturing nor sub-lithostatic overpressure regimes are required to produce that HDB structure. The textural similarities between the Mail Arrouy case and other HDB presented across the world question the way we interpret hydrothermal breccia structures as proxies for fluid overpressure, and also shows how reactive fluid-rock interaction can be misleading in geological interpretations.

## Acknowledgement

This work is funded by the project TXM-R2 (Institut Carnot ISiFOR), S.C. and N.B. are funded through the isite-E2S, supported by the ANR PIA and the Région Nouvelle-Aquitaine. We thank Arnaud Proietti for the EBSD analyses and the help for the data processing. We thank Benoit Vincent for the discussions that helped to improve the manuscript. DK acknowledged funding by the Bavarian Ministry of Science and Art (StMWK) funded project "langfristig" of the Geothermal Alliance Bavaria (GAB).

Figure caption:

Figure 1: Hand specimen of hydrothermal dolomite breccia in (a) Canada (Haeri-Ardakani et al., 2013), (c) Hungary (Garaguly et al., 2018), (d) French Alps (Barale et al., 2016), (e) Oman (Beckert et al., 2015). (e, f, g) Zoom in at the clast-cement interface with location of rough contact (black arrows).

Figure 2: a) Structural map of the Pyrenees. NPFT: North-Pyrenean Frontal Thrust, NPF: North-Pyrenean Fault, SPF: South-Pyrenean Fault, SPFT: South Pyrenean Frontal Thrust (Vauchez et al., 2013). b) Structural map of the Chaînons Béarnais region (Castéras et al., 1970; Corre et al., 2016; Lagabrielle et al., 2010). Location of the studied outcrop in yellow star.

Figure 3: a) Field view of a dolomite breccia structure in the Mano Formation. (b,c) Closer view of dolomite breccia structure with three dolomite textures highlighted in (c). (d,e) Scan of a polished slab (d) and its interpretative sketch (e). (f, g, h) Zoom in on dolomite clasts, oxides, and matrix.

Figure 4: Zoom in on the interfaces between clast and cement (a, b, c), and cement and matrix (d). Arrows are pointing out the roughness of the surface. See location in Figure 3e. e) Diagenetic phases of the HDB with reported temperatures from fluid inclusion microthermometry after Motte et al. (2021). Older dolomite at the top and younger at the bottom.

Figure 5: a) Photograph of a polished hydrothermal dolomite breccia sample, with location of the areas used for image analysis. (b, d, f) Close view of the three areas selected for image analysis. (c, e, g) Corresponding phase segmentation and statistical data (c).

Figure 6: Backscattered image of the matrix (a, b) and the clasts (c, d).

Figure 7: High resolution scan of the polished slab in Fig. 3d and e (a), with sketch of the different dolomite types based on the colour and texture (b), mineralogical phase map (c) and crystal size map (d, colour scale relates to circle equivalent diameter in µm). Images c) (Phase map) and d) (dolomite crystal size) are overlain with band contrast (quality factor that describes the average intensity of the Kikuchi bands). (e) Dolomite crystal axis orientations represented on stereographs as pole concentration (lower hemisphere) based on the area of interest reported on Fig. 3e. High concentration in red and low in blue.

Figure 8: Electron backscatter diffraction (EBSD) maps (see location in Figure 3e): a) Mineral phase map overlain in semi-transparency with band contrast (quality factor that describes the average intensity of the Kikuchi bands). b) Dolomite crystal size (colour scale relates to circle equivalent diameter in µm). c) Grain boundaries angle of dolomite. d) Grain reference orientation deviation (GROD), reported in red if superior to 20°. Note that grain reference orientation deviation above 20° will be in red. The non-indexed pixels on the left-hand side of the figure are probably the result of a bad polished surface and impurities on the surface of the thin section.

Figure 9: Results of numerical modelling of the progressive replacement of the initial breccia structure by coarse dolomite cement. The simulation box is 2.2x2.2 mm. Each diagram in the same line is a snapshot of the same simulation at a given value of the Péclet number (advection rate/diffusion rate), located by red dots at different computation step. White to black colour scale represents the percent of reaction, and we consider that only the black colour account for replaced minerals. The two last columns on the right-hand side are alternate representations of the last step of the simulation that emphasize the morphology of the replacement front.

Figure 10: Sketch illustrating a conceptual model leading to the complete replacement of the initial sedimentary breccia structure (in orange) as coarse cement (in white), mimicking the texture of hydrothermal dolomite breccia (as fluid overpressure). a) Original sedimentary breccia dolomite structure with oxides (red). b) Fluid infiltration through grain boundaries (blue) of a hot fluid (300°C) in the cold host rock (200°C). c) Step of recrystallization process triggered by temperature gradient, that pushes the oxides away. Reaction stops when the temperature gradient becomes too low.

Fig. A1: Creation of a mesh usable for numerical simulation in the ELLE environment from the grain boundaries angles maps from EBSD (location Figure 6b). Black clasts are composed by small grain size less than 50 µm (circle equivalent diameter). For the simulation, the porosity of the grains is fixed to 4% based on BSE image analysis (Fig. 8). Right side has been changed to allow fluid to infiltrate rather than to be blocked by a clast.

Table caption:

Table 1: model parameters for simulations

# 1 References

Amrouch, K., Beaudoin, N., Lacombe, O., Bellahsen, N., Daniel, J.-M., 2011. Paleostress magnitudes in folded sedimentary rocks. Geophys. Res. Lett. 38, n/a-n/a. https://doi.org/10.1029/2011GL048649.

Bach, W., Paulick, H., Garrido, C.J., Ildefonse, B., Meurer, W.P., Humphris, S.E., 2006. Unraveling the sequence of serpentinization reactions: petrography, mineral chemistry, and petrophysics of serpentinites from MAR 15°N (ODP Leg 209, Site 1274). Geophys. Res. Lett. 33. https://doi.org/10.1029/2006GL025681.

Baisch, S., 2020. Inferring In Situ Hydraulic Pressure From Induced Seismicity Observations: An Application to the Cooper Basin (Australia) Geothermal Reservoir. J. Geophys. Res. Solid Earth 125, 341. https://doi.org/10.1029/2019JB019070.

Barale, L., Bertok, C., d’Atri, A., Domini, G., Martire, L., Piana, F., 2013. Hydrothermal dolomitization of the carbonate Jurassic succession in the Provençal and Subbriançonnais Domains (Maritime Alps, North-Western Italy). Comptes Rendus Geoscience 345, 47–53. https://doi.org/10.1016/j.crte.2012.10.015.

Barale, L., Bertok, C., Salih Talabani, N., d'Atri, A., Martire, L., Piana, F., Préat, A., 2016. Very hot, very shallow hydrothermal dolomitization: An example from the Maritime Alps (north-west Italy-south-east France). Sedimentology 63, 2037–2065. https://doi.org/10.1111/sed.12294.

Beaudoin, N., Lacombe, O., Bellahsen, N., Amrouch, K., Daniel, J.-M., 2014. Evolution of pore-fluid pressure during folding and basin contraction in overpressured reservoirs: Insights from the Madison–Phosphoria carbonate formations in the Bighorn Basin (Wyoming, USA). Marine and Petroleum Geology 55, 214–229. https://doi.org/10.1016/j.marpetgeo.2013.12.009.

Beckert, J., Vandeginste, V., John, C.M., 2015. Exploring the geological features and processes that control the shape and internal fabrics of late diagenetic dolomite bodies (Lower Khuff equivalent – Central Oman Mountains). Marine and Petroleum Geology 68, 325–340. https://doi.org/10.1016/j.marpetgeo.2015.08.038.

Bjørlykke, K., Middleton, G.V., 2003. Compaction (consolidation) of sediments. Encyclopedia of sediments and sedimentary rocks: Dordrecht, Netherlands, Kluwer Academic Publishers, 161–168.

Bons, P.D., Elburg, M.A., Gomez-Rivas, E., 2012. A review of the formation of tectonic veins and their microstructures. Journal of Structural Geology 43, 33–62. https://doi.org/10.1016/j.jsg.2012.07.005.

Bons, P.D., Koehn, D., Jessell, M.W., 2008a. Microdynamics simulation. Springer, Berlin, xix, 405.

Bons, P.D.D., Koehn, D., Jessell, M.W., 2008b. Microdynamics Simulation. Springer Berlin Heidelberg, Berlin, Heidelberg, 19 pp.

Carman, P.C., 1937. Fluid flow through granular beds. PhD thesis.

Castéras, M., Canérot, J., Paris, J., Tisin, D., Azambre, M., Alimen, H., 1970. Carte géologique de la France au 1/50 000: Feuille d’Oloron Sainte Marie.

Centrella, S., Beaudoin, N.E., Derluyn, H., Motte, G., Hoareau, G., Lanari, P., Piccoli, F., Pecheyran, C., Callot, J.-P., 2020. Micro-scale chemical and physical patterns in an interface of hydrothermal dolomitization reveals the governing transport mechanisms in nature: case of the Layens anticline, Pyrenees, France. Sedimentology. https://doi.org/10.1111/sed.12808.

Chen, D., Qing, H., Yang, C., 2004. Multistage hydrothermal dolomites in the Middle Devonian (Givetian) carbonates from the Guilin area, South China. Sedimentology 51, 1029–1051. https://doi.org/10.1111/j.1365-3091.2004.00659.x.

Clerc, C., Lahfid, A., Monié, P., Lagabrielle, Y., Chopin, C., Poujol, M., Boulvais, P., Ringenbach, J.-C., Masini, E., St Blanquat, M. de, 2015. High-temperature metamorphism during extreme thinning of the continental crust: a reappraisal of the North Pyrenean passive paleomargin. Solid Earth 6, 643–668. https://doi.org/10.5194/se-6-643-2015.

Cobbold, P.R., Rodrigues, N., 2007. Seepage forces, important factors in the formation of horizontal hydraulic fractures and bedding-parallel fibrous veins (?beef? and ?cone-in-cone?). Geofluids 7, 313–322. https://doi.org/10.1111/j.1468-8123.2007.00183.x.

Cornet, F.H., Li, L., Hulin, J.-P., Ippolito, I., Kurowski, P., 2003. The hydromechanical behaviour of a fracture: an in situ experimental case study. International Journal of Rock Mechanics and Mining Sciences 40, 1257–1270. https://doi.org/10.1016/S1365-1609(03)00120-5.

Corre, B., Lagabrielle, Y., Labaume, P., Fourcade, S., Clerc, C., Ballèvre, M., 2016. Deformation associated with mantle exhumation in a distal, hot passive margin environment: New constraints from the Saraillé Massif (Chaînons Béarnais, North-Pyrenean Zone). Comptes Rendus Geoscience 348, 279–289. https://doi.org/10.1016/j.crte.2015.11.007.

Davies, G.R., Smith, L.B., 2006. Structurally controlled hydrothermal dolomite reservoir facies: An overview. Bulletin 90, 1641–1690. https://doi.org/10.1306/05220605164.

Flekkøy, E.G., Malthe-Sørenssen, A., Jamtveit, B., 2002. Modeling hydrofracture. J. Geophys. Res. 107, 648. https://doi.org/10.1029/2000JB000132.

Garaguly, I., Varga, A., Raucsik, B., Schubert, F., Czuppon, G., Frei, R., 2018. Pervasive early diagenetic dolomitization, subsequent hydrothermal alteration, and late stage hydrocarbon accumulation in a Middle Triassic carbonate sequence (Szeged Basin, SE Hungary). Marine and Petroleum Geology 98, 270–290. https://doi.org/10.1016/j.marpetgeo.2018.07.024.

Ghani, I., Koehn, D., Toussaint, R., Passchier, C.W., 2013. Dynamic development of hydrofracture. Pure and Applied Geophysics 170, 1685–1703.

Grimaldi, M.-H., 1988. La dolomie tidale du Jurassique terminal des Pyrénées occidentales. Sédimentologie, diagénèse polyphasée et contexte dynamique. Université de Pau.

Gudmundsson, A., 2001. Fluid overpressure and flow in fault zones: field measurements and models. Tectonophysics 336, 183–197.

Guo, C., Chen, D., Qing, H., Dong, S., Li, G., Wang, D., Qian, Y., Liu, C., 2016. Multiple dolomitization and later hydrothermal alteration on the Upper Cambrian-Lower Ordovician carbonates in the northern Tarim Basin, China. Marine and Petroleum Geology 72, 295–316. https://doi.org/10.1016/j.marpetgeo.2016.01.023.

Haeri-Ardakani, O., Al-Aasm, I., Coniglio, M., 2013. Petrologic and geochemical attributes of fracture-related dolomitization in Ordovician carbonates and their spatial distribution in southwestern Ontario, Canada. Marine and Petroleum Geology 43, 409–422. https://doi.org/10.1016/j.marpetgeo.2012.12.006.

Harlov, D.E., Austrheim, H. (Eds.), 2013. Metasomatism and the Chemical Transformation of Rock. Springer Berlin Heidelberg, Berlin, Heidelberg.

Hendry, J.P., Gregg, J.M., Shelton, K.L., Somerville, I.D., Crowley, S.F., 2015. Origin, characteristics and distribution of fault-related and fracture-related dolomitization: Insights from Mississippian carbonates, Isle of Man. Sedimentology 62, 717–752. https://doi.org/10.1111/sed.12160.

Iannace, A., Gasparrini, M., Gabellone, T., Mazzoli, S., 2012. Late Dolomitization in basinal limestones of the southern Apennines fold and thrust belt (Italy). Oil Gas Sci. Technol. – Rev. IFP Energies nouvelles 67, 59–75. https://doi.org/10.2516/ogst/2011166.

Incerpi, N., Manatschal, G., Martire, L., Bernasconi, S.M., Gerdes, A., Bertok, C., 2020. Characteristics and timing of hydrothermal fluid circulation in the fossil Pyrenean hyperextended rift system: new constraints from the Chaînons Béarnais (W Pyrenees). Int J Earth Sci (Geol Rundsch) 110, 1. https://doi.org/10.1007/s00531-020-01852-6.

Iriarte, E., López-Horgue, M.A., Schroeder, S., Caline, B., 2012. Interplay between fracturing and hydrothermal fluid flow in the Asón Valley hydrothermal dolomites (Basque–Cantabrian Basin, Spain). Geological Society, London, Special Publications 370, 207–227. https://doi.org/10.1144/SP370.10.

Izquierdo-Llavall, E., Menant, A., Aubourg, C., Callot, J.-P., Hoareau, G., Lahfid, A., Camps, P., Pere, E., 2020. Pre-orogenic folds and syn-orogenic basement tilts in an inverted hyperextended margin : the northern Pyrenees case study. Tectonics 39.

Jébrak, M., 1997. Hydrothermal breccias in vein-type ore deposits: A review of mechanisms, morphology and size distribution. Ore Geology Reviews 12, 111–134.

Jonas, L., Müller, T., Dohmen, R., Baumgartner, L., Putlitz, B., 2015. Transport-controlled hydrothermal replacement of calcite by Mg-carbonates. Geology 43, 779–782. https://doi.org/10.1130/G36934.1.

Jonas, L., Müller, T., Dohmen, R., Immenhauser, A., Putlitz, B., 2017. Hydrothermal replacement of biogenic and abiogenic aragonite by Mg-carbonates – Relation between textural control on effective element fluxes and resulting carbonate phase. Geochimica et Cosmochimica Acta 196, 289–306. https://doi.org/10.1016/j.gca.2016.09.034.

Kelka, U., 2017. Pattern Formation in Mississippi Valley-Type Deposits - Identifying one of Nature's Fundamental Processes in Geologic Systems. PhD thesis.

Kelka, U., Koehn, D., Beaudoin, N., 2015. Zebra pattern in rocks as a function of grain growth affected by second-phase particles. Front. Phys. 3, 201. https://doi.org/10.3389/fphy.2015.00074.

Koehn, D., Piazolo, S., Beaudoin, N.E., Kelka, U., Spruženiece, L., Putnis, C.V., Toussaint, R., 2021. Relative rates of fluid advection, elemental diffusion and replacement govern reaction front patterns. Earth and Planetary Science Letters 565, 116950. https://doi.org/10.1016/j.epsl.2021.116950.

Koehn, D., Piazolo, S., Sachau, T., Toussaint, R., 2020. Fracturing and porosity channeling in fluid overpressure zones in the shallow Earth's crust. Geofluids 2020, 1–17. https://doi.org/10.1155/2020/7621759.

Labaume, P., Teixell, A., 2020. Evolution of salt structures of the Pyrenean rift (Chaînons Béarnais, France): From hyper-extension to tectonic inversion. Tectonophysics 785. https://doi.org/10.1016/j.tecto.2020.228451.

Lafay, R., Baumgartner, L.P., Schwartz, S., Picazo, S., Montes-Hernandez, G., Vennemann, T., 2017. Petrologic and stable isotopic studies of a fossil hydrothermal system in ultramafic environment (Chenaillet ophicalcites, Western Alps, France): Processes of carbonate cementation. Lithos 294-295, 319–338. https://doi.org/10.1016/j.lithos.2017.10.006.

Lagabrielle, Y., Labaume, P., Saint Blanquat, M.d., 2010. Mantle exhumation, crustal denudation, and gravity tectonics during Cretaceous rifting in the Pyrenean realm (SW Europe): Insights from the geological setting of the lherzolite bodies. Tectonics 29, n/a-n/a. https://doi.org/10.1029/2009TC002588.

Lax, P., Wendroff, B., 1960. Systems of conservation laws. Communications on Pure and Applied Mathematics 13, 217–237.

Lenoble, J.-L., 1992. Les plates-formes carbonatées ouest pyrénéennes du Dogger à l'Albien. PhD. Toulouse, 447 pp.

López-Horgue, M.A., Iriarte, E., Schröder, S., Fernández-Mendiola, P.A., Caline, B., Corneyllie, H., Frémont, J., Sudrie, M., Zerti, S., 2010. Structurally controlled hydrothermal dolomites in Albian carbonates of the Asón valley, Basque Cantabrian Basin, Northern Spain. Marine and Petroleum Geology 27, 1069–1092. https://doi.org/10.1016/j.marpetgeo.2009.10.015.

Malaroda, R., 1999. L’Argentera meridionale – Memoria illustrativa della “Geological Map of Southern Argentera Massif (Maritime Alps) 1:25 000”. Mem. Soc. Geol. Ital. 51-52, 241–331.

Mattes, B.W., Mountjoy, E.W., 1980. Burial Dolomitization of the Upper Devonian Miette Buildup, Jasper National Park, Alberta. The Society of Economic Paleontologists and Mineralogists 28, 259–297.

Morrow, D.W., 1982. Descriptive field classification of sedimentary and diagenetic breccia fabrics in carbonate rocks. Bulletin of Canadian Petroleum Geology 30, 227–229.

Motte, G., Hoareau, G., Callot, J.-P., Révillon, S., Piccoli, F., Calassou, S., Gaucher, E.C., 2021. Rift and salt-related multi-phased dolomitization: example from the northwestern Pyrenees. Marine and Petroleum Geology 126. https://doi.org/10.1016/j.marpetgeo.2021.104932.

Mouthereau, F., Filleaudeau, P.-Y., Vacherat, A., Pik, R., Lacombe, O., Fellin, M.G., Castelltort, S., Christophoul, F., Masini, E., 2014. Placing limits to shortening evolution in the Pyrenees: Role of margin architecture and implications for the Iberia/Europe convergence. Tectonics 33, 2283–2314. https://doi.org/10.1002/2014TC003663.

Nader, F.H., Swennen, R., Ellam, R., 2004. Reflux stratabound dolostone and hydrothermal volcanism-associated dolostone: a two-stage dolomitization model (Jurassic, Lebanon). Sedimentology 51, 339–360. https://doi.org/10.1111/j.1365-3091.2004.00629.x.

O'Neil, J.R., 1977. Stable isotopes in mineralogy. Physics and Chemistry of Minerals 2, 105–123.

O'Neil, J.R., Taylor, H.P., 1967. The oxygen isotope and cation exchange chemistry of feldspars. The American Mineralogist 52, 1414–1437.

Passelègue, F.X., Fabbri, O., Dubois, M., Ventalon, S., 2014. Fluid overpressure along an Oligocene out-of-sequence thrust in the Shimanto Belt, SW Japan. Journal of Asian Earth Sciences 86, 12–24. https://doi.org/10.1016/j.jseaes.2013.10.024.

Peacock, D.C.P., Rotevatn, A., Sanderson, D.J., 2019. Brecciation driven by changes in fluid column heights. Terra Nova 31, 76–81. https://doi.org/10.1111/ter.12371.

Piazolo, S., Bons, P.D., Griera, A., Llorens, M.-G., Gomez-Rivas, E., Koehn, D., Wheeler, J., Gardner, R., Godinho, J., Evans, L., Lebensohn, R.A., Jessell, M.W., 2019. A review of numerical modelling of the dynamics of microstructural development in rocks and ice: Past, present and future. Journal of Structural Geology 125, 111–123. https://doi.org/10.1016/j.jsg.2018.05.025.

Pironon, J., 2004. Fluid inclusions in petroleum environments: analytical procedure for PTX reconstruction. Acta Petrologica Sinica 20, 1333–1342.

Putnis, A., Austrheim, H., 2013. Mechanisms of Metasomatism and Metamorphism on the Local Mineral Scale: The Role of Dissolution-Reprecipitation During Mineral Re-equilibration, in: Harlov, D.E., Austrheim, H. (Eds.), Metasomatism and the Chemical Transformation of Rock, vol. 294. Springer Berlin Heidelberg, Berlin, Heidelberg, pp. 141–170.

Roure, F., Andriessen, P., Callot, J.P., Faure, J.L., Ferket, H., Gonzales, E., Guilhaumou, N., Lacombe, O., Malandain, J., Sassi, W., Schneider, F., Swennen, R., Vilasi, N., 2010. The use of palaeo-thermo-barometers and coupled thermal, fluid flow and pore-fluid pressure modelling for hydrocarbon and reservoir prediction in fold and thrust belts. Geological Society, London, Special Publications 348, 87–114. https://doi.org/10.1144/SP348.6.

Salardon, R., Carpentier, C., Bellahsen, N., Pironon, J., France-Lanord, C., 2017. Interactions between tectonics and fluid circulations in an inverted hyper-extended basin: Example of mesozoic carbonate rocks of the western North Pyrenean Zone (Chaînons Béarnais, France). Marine and Petroleum Geology 80, 563–586. https://doi.org/10.1016/j.marpetgeo.2016.11.018.

Sibson, R.H., 2012. Reverse fault rupturing: competition between non-optimal and optimal fault orientations. Geological Society, London, Special Publications 367, 39–50. https://doi.org/10.1144/SP367.4.

Szymczak, P., Ladd, A.J.C., 2009. Wormhole formation in dissolving fractures. J. Geophys. Res. 114, 433. https://doi.org/10.1029/2008JB006122.

Szymczak, P., Ladd, A.J.C., 2013. Interacting length scales in the reactive-infiltration instability. Geophys. Res. Lett. 40, 3036–3041. https://doi.org/10.1002/grl.50564.

Szymczak, P., Ladd, A.J.C., 2014. Reactive-infiltration instabilities in rocks. Part 2. Dissolution of a porous matrix. J. Fluid Mech. 738, 591–630. https://doi.org/10.1017/jfm.2013.586.

Thomas, J., Frost, R.R., Harvey, R.D., 1973. Thermal conductivity of carbonate rocks. Engineering Geology 7, 3–12.

Tugend, J., Manatschal, G., Kusznir, N.J., 2015. Spatial and temporal evolution of hyperextended rift systems: Implication for the nature, kinematics, and timing of the Iberian-European plate boundary. Geology 43, 15–18. https://doi.org/10.1130/G36072.1.

Vacherat, A., Mouthereau, F., Pik, R., Bernet, M., Gautheron, C., Masini, E., Le Pourhiet, L., Tibari, B., Lahfid, A., 2014. Thermal imprint of rift-related processes in orogens as recorded in the Pyrenees. Earth and Planetary Science Letters 408, 296–306. https://doi.org/10.1016/j.epsl.2014.10.014.

Vass, A., Koehn, D., Toussaint, R., Ghani, I., Piazolo, S., 2014. The importance of fracture-healing on the deformation of fluid-filled layered systems. Journal of Structural Geology 67, 94–106. https://doi.org/10.1016/j.jsg.2014.07.007.

Vauchez, A., Clerc, C., Bestani, L., Lagabrielle, Y., Chauvet, A., Lahfid, A., Mainprice, D., 2013. Preorogenic exhumation of the North Pyrenean Agly massif (Eastern Pyrenees-France). Tectonics 32, 95–106. https://doi.org/10.1002/tect.20015.

Wang, Y., Liu, L., Hu, Q., Hao, L., Wang, X., Sheng, Y., 2020. Nanoscale Pore Network Evolution of Xiamaling Marine Shale during Organic Matter Maturation by Hydrous Pyrolysis. Energy Fuels 34, 1548–1563. https://doi.org/10.1021/acs.energyfuels.9b03686.

Wang, Y., Liu, Z., Song, G., Zhang, Y., Zhu, C., Li, S., Wang, P., Tang, P., 2019. Genesis of lacustrine carbonate breccia and its significance for hydrocarbon exploration in Yingxi region, Qaidam Basin, NW China. Petroleum Exploration and Development 46, 104–112. https://doi.org/10.1016/S1876-3804(19)30009-6.

Xiong, J., Lin, H., Ding, H., Pei, H., Rong, C., Liao, W., 2020. Investigation on thermal property parameters characteristics of rocks and its influence factors. Natural Gas Industry B 7, 298–308. https://doi.org/10.1016/j.ngib.2020.04.001.

Yanagisawa, K., Redon-Angeles, J.C., Ishizawa, N., Oishi, S., 1999. Topoaxial replacement of chlorapatite by hydroxyapatite during hydrothermal ion exchange. American Mineralogist 84, 1861–1869.

Zoback, M.D., Townend, J., 2001. Implications of hydrostatic pore pressure and high crustal strength for the deformation of intraplate lithosphere. Tectonophysics 336, 19–30.

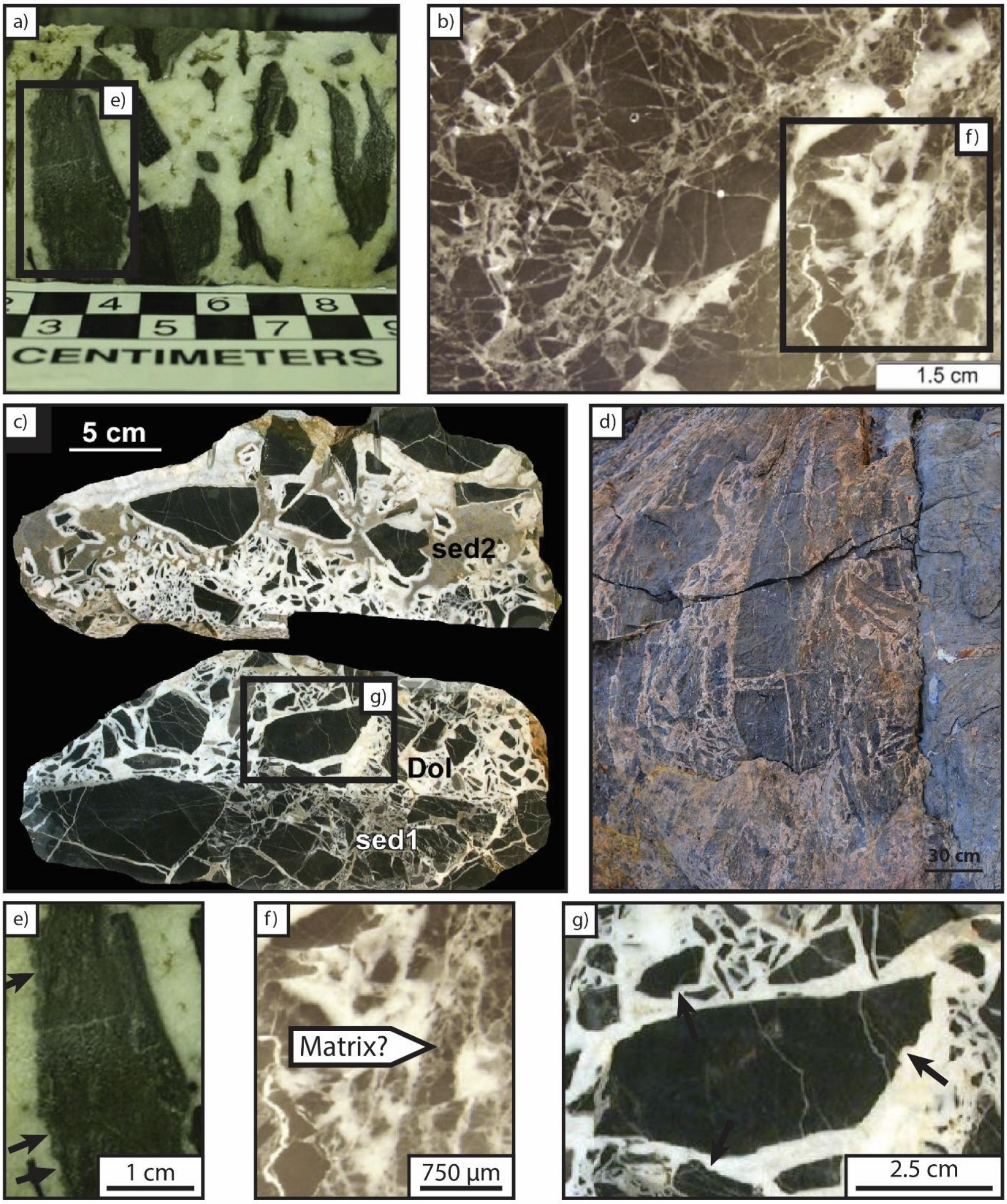

Figure 1: Hand specimen of hydrotherml dolomite breccia in (a) Canada (modified from Haeri-Ardakani et al. 2013), (b) Hungary (modified from Garaguly et al. 2018), (c) French Alps (modified from Barale et al. 2016), (d) Oman (modified from Beckert et al. 2015). (e, f, g) Zoom at the clast-cement interface with location of rough contact (black arrows).

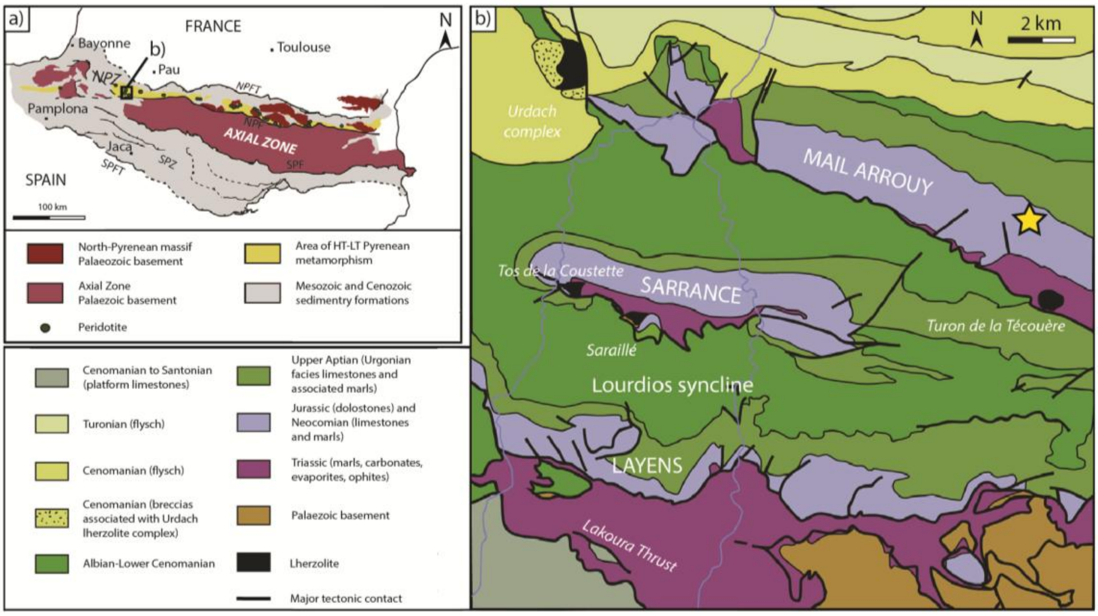

Fig. 2: a) Structural map of the Pyrenees. NPFT: North-Pyrenean Frontal Thrust, NPF: North-Pyrenean Fault, SPF: South-Pyrenean Fault, SPFT: South Pyrenean Frontal Thrust (after Vauchez et al., 2013). b) Structural map of the Chaînons Béarnais region (modified after Castéras, 1970; Corre et al., 2016; Lagabrielle et al., 2010). Location of the studied outcrop in yellow star.

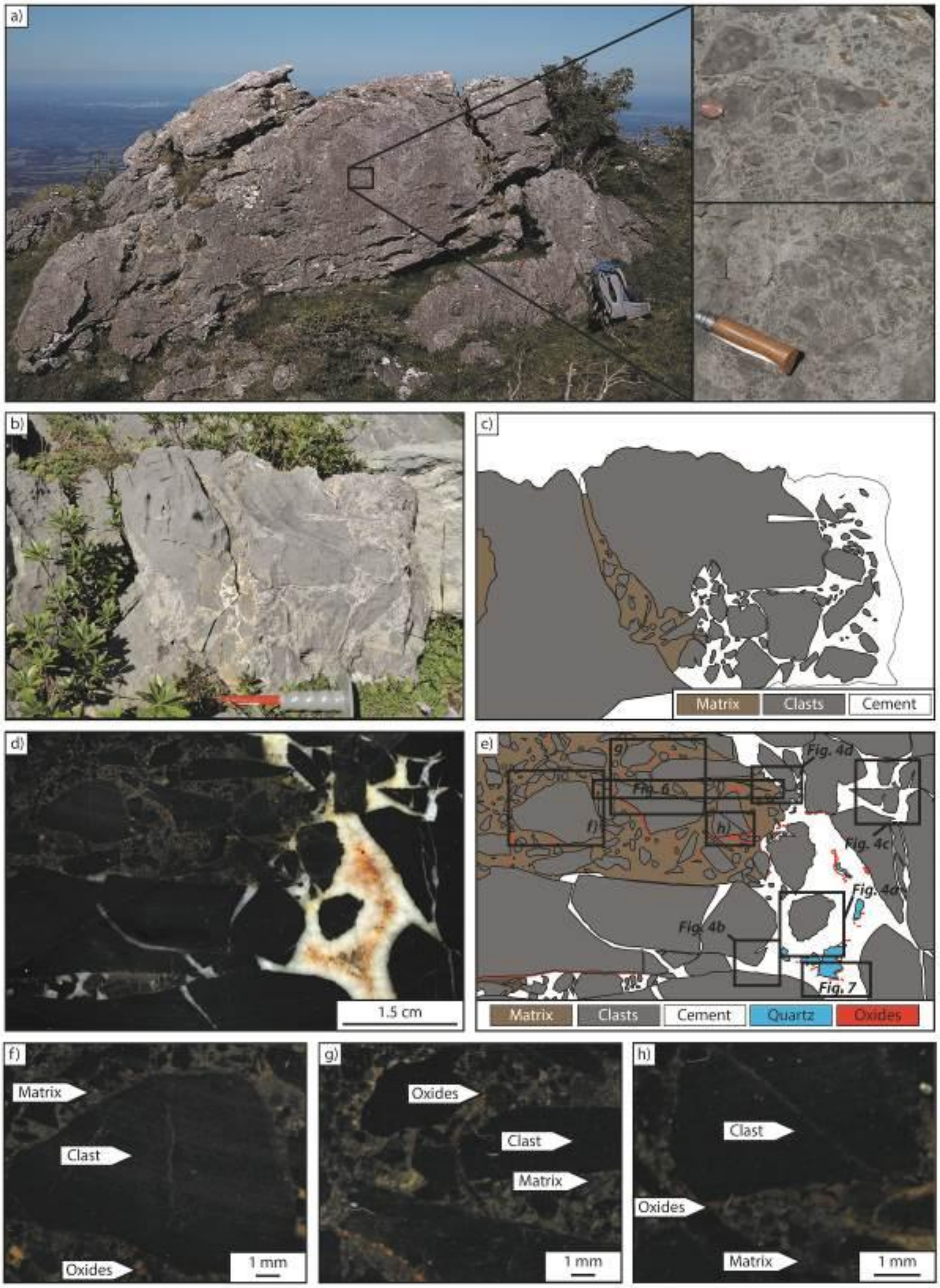

Fig. 3: a) Field view of a dolomite breccia structure in the Mano Formation. (b,c) Closer view of dolomite breccia structure with three dolomite textures highlighted in (c). (d,e) Scan of a polished slab (d) and its interpretative sketch (e). (f, g, h) Zoom on dolomite clasts, oxides, and matrix.

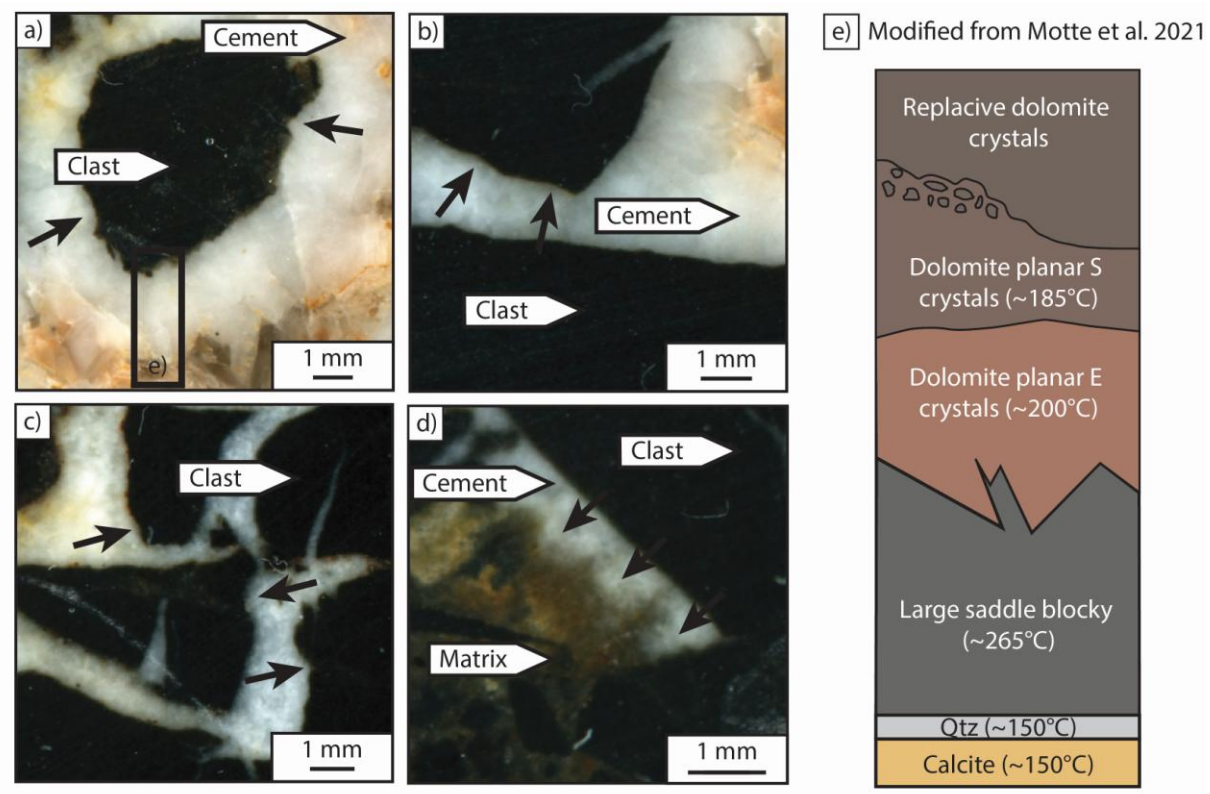

Fig. 4: Zoom on the interfaces between clast and cement (a, b, c), and cement and matrix (d). Arrows are pointing roughness surface. See location in Figure 3e. e) Diagenetic phases of the HDB with temperature from fluid inclusion micro thermometry after Motte et al. (2021). Older dolomite at the top and younger at the bottom.

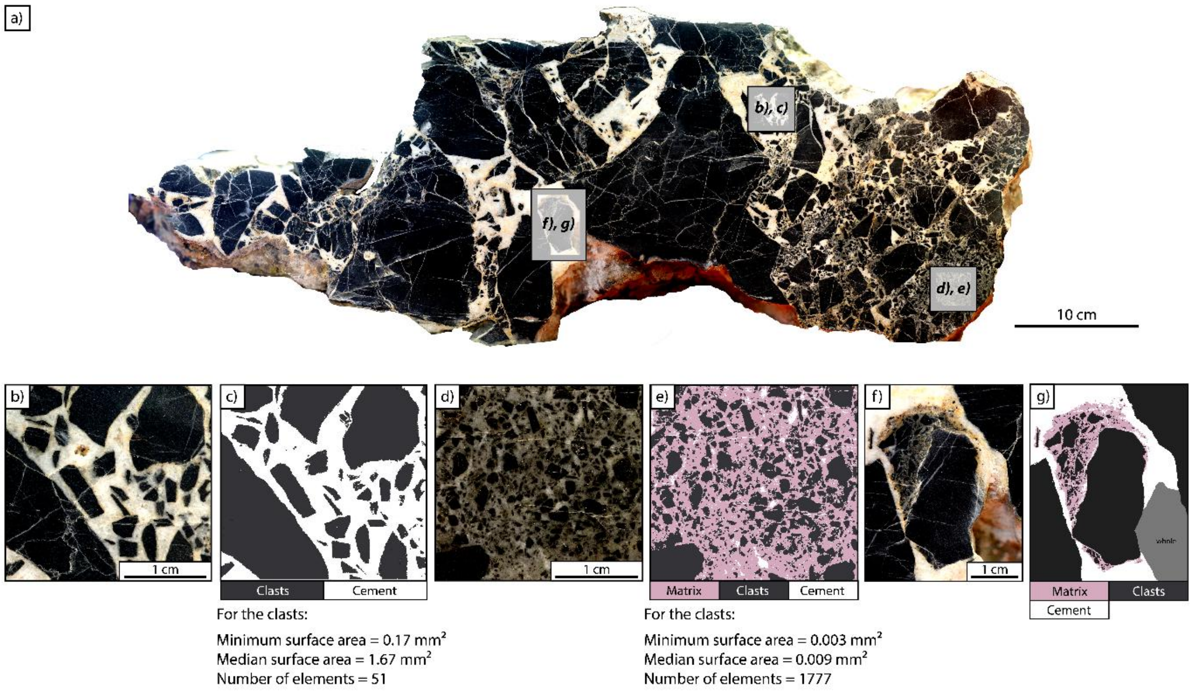

Fig. 5: a) Photograph of a polished hydrothermal dolomite breccia sample, with location of the areas used for image analysis. (b,d,f) Close view of the three areas selected for image analysis. (c,e,g) Corresponding phase segmentation and statistical data (c).

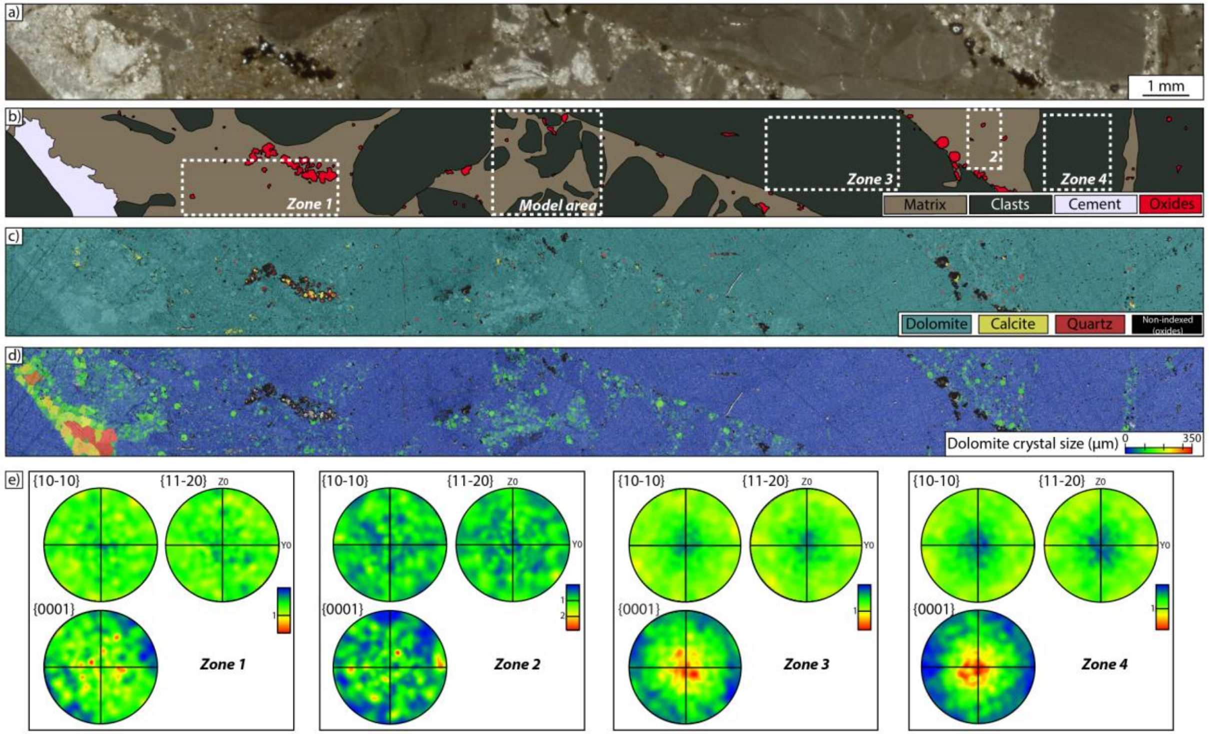

Fig. 6: High resolution scan of the polished slab presented in Fig. 3d and e (a), with sketch of the different dolomite types based on the colour and texture (b), mineralogical phase map (c) and crystal size map (d, colour scale relates to circle equivalent diameter in µm). Images c) and d) are overlain with band contrast (quality factor that describes the average intensity of the Kikuchi bands). (e) Dolomite crystal axis orientations represented on stereographs as pole concentration (lower hemisphere) based on the area of interest reported on Fig. 3e. High concentration in red and low in blue.

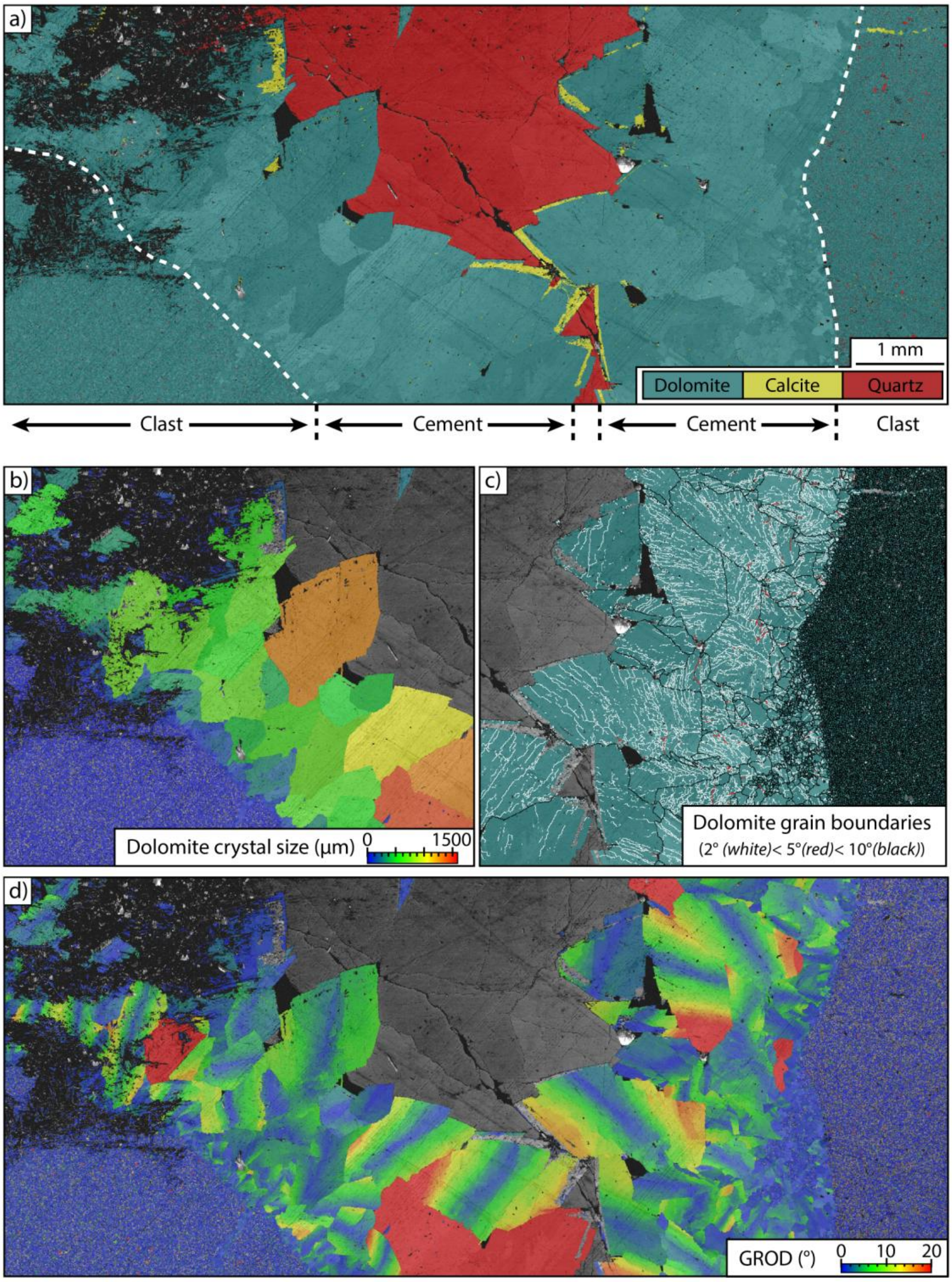

Fig. 7: Electron backscatter diffraction (EBSD) maps (see location in Figure 3e): a) Mineral phase map overlain in semi-transparency with band contrast (quality factor that describes the average intensity of the Kikuchi bands). b) Dolomite crystal size (colour scale relates to circle equivalent diameter in µm). c) Grain boundaries angle of dolomite. d) Grain reference orientation deviation (GROD), reported in red if superior to 20°. Note that grain reference orientation deviation above 20° will be in red. The non-indexed pixels on the left-hand side of the figure are probably the result of a bad polished surface and impurities on the surface of the thin section.

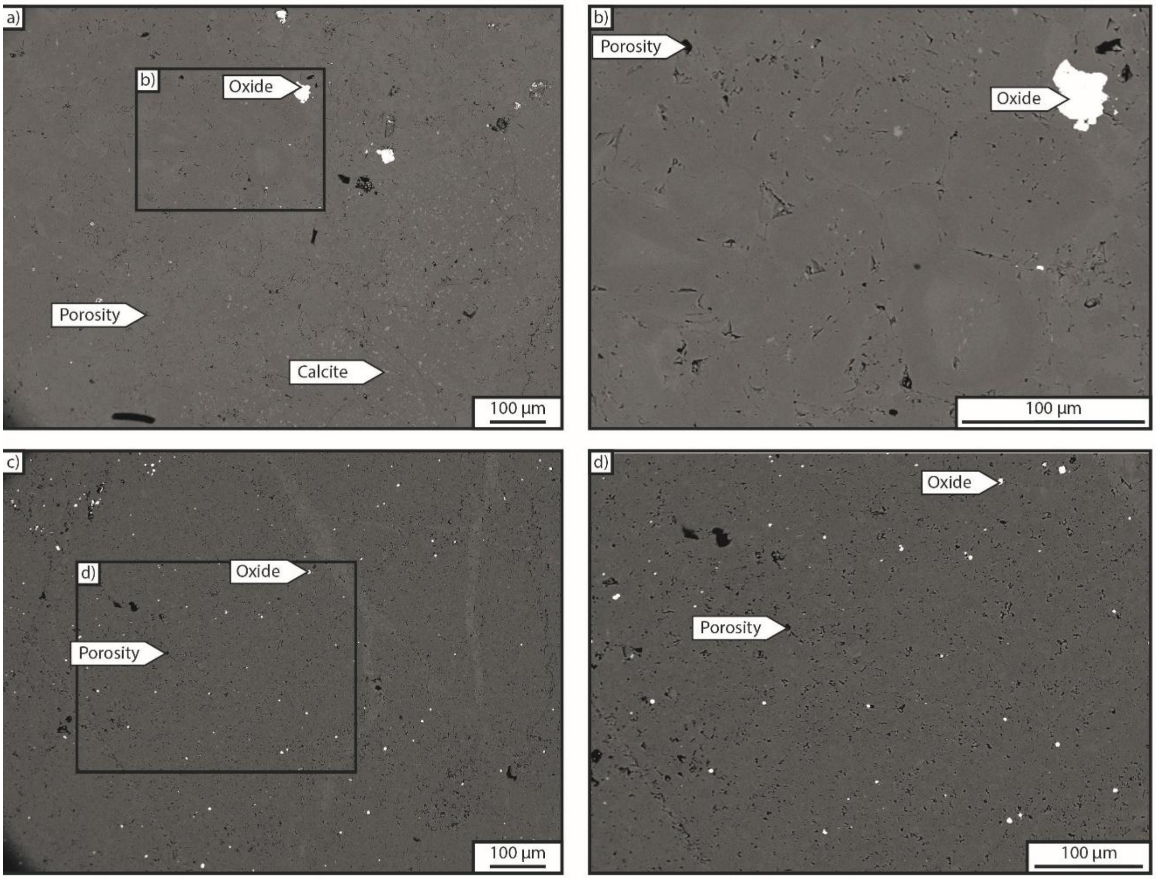

Fig. 8: Backscattered image of the matrix (a, b) and the clasts (c, d).

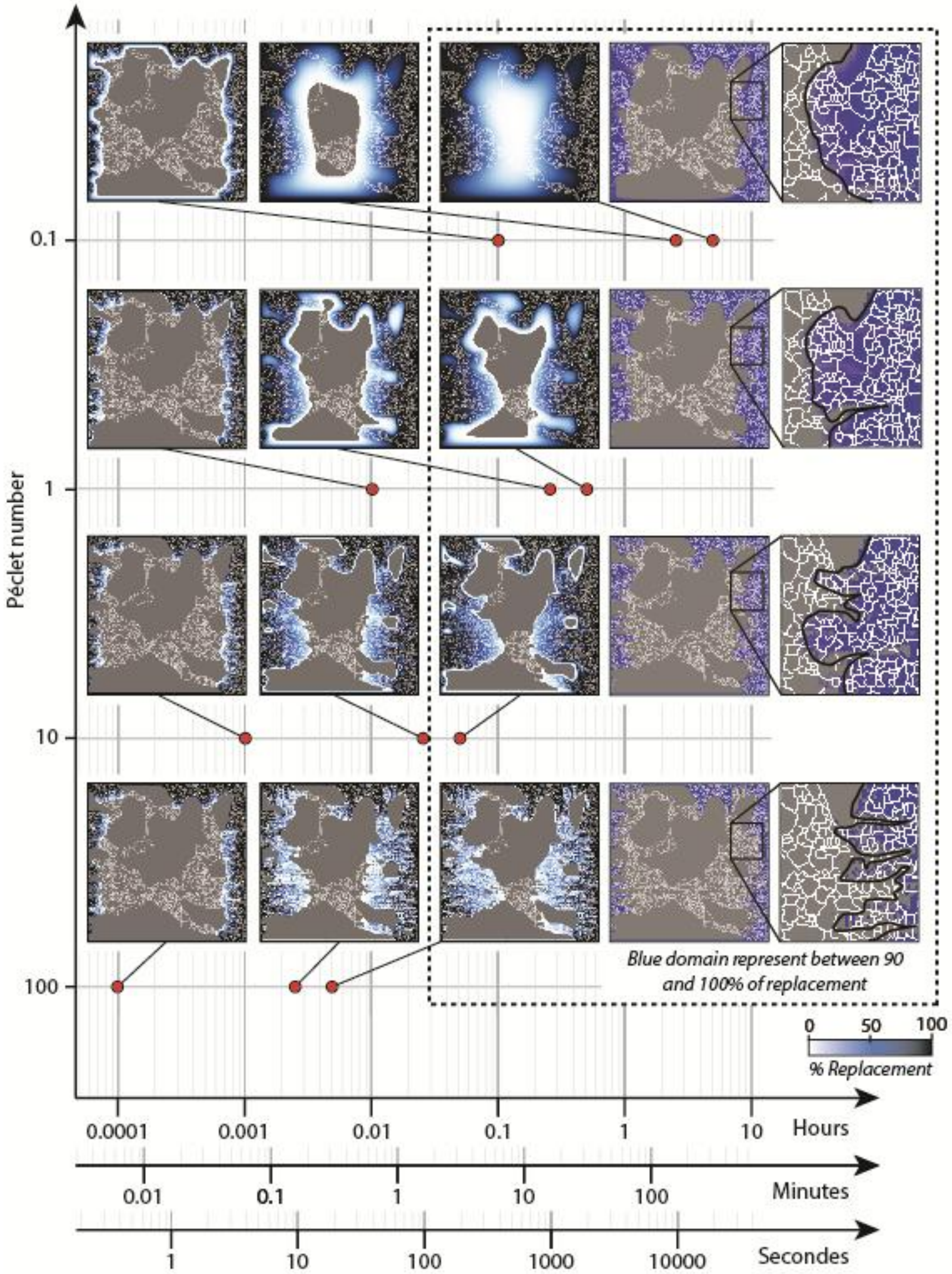

Fig. 9: Results of numerical modelling of the progressive replacement of the initial breccia structure by coarse dolomite cement. The simulation box is 2.2x2.2 mm. Each diagram in the same line is a snapshot of the same simulation at a given value of the Péclet number (advection rate/diffusion rate), located by red dots at different computation step. White to black colour scale represents the % of reaction, and we consider that only the black colour account for replaced minerals. The two last

columns on the right-hand side are alternate representations of the last step of the simulation that emphasize the morphology of the replacement front.

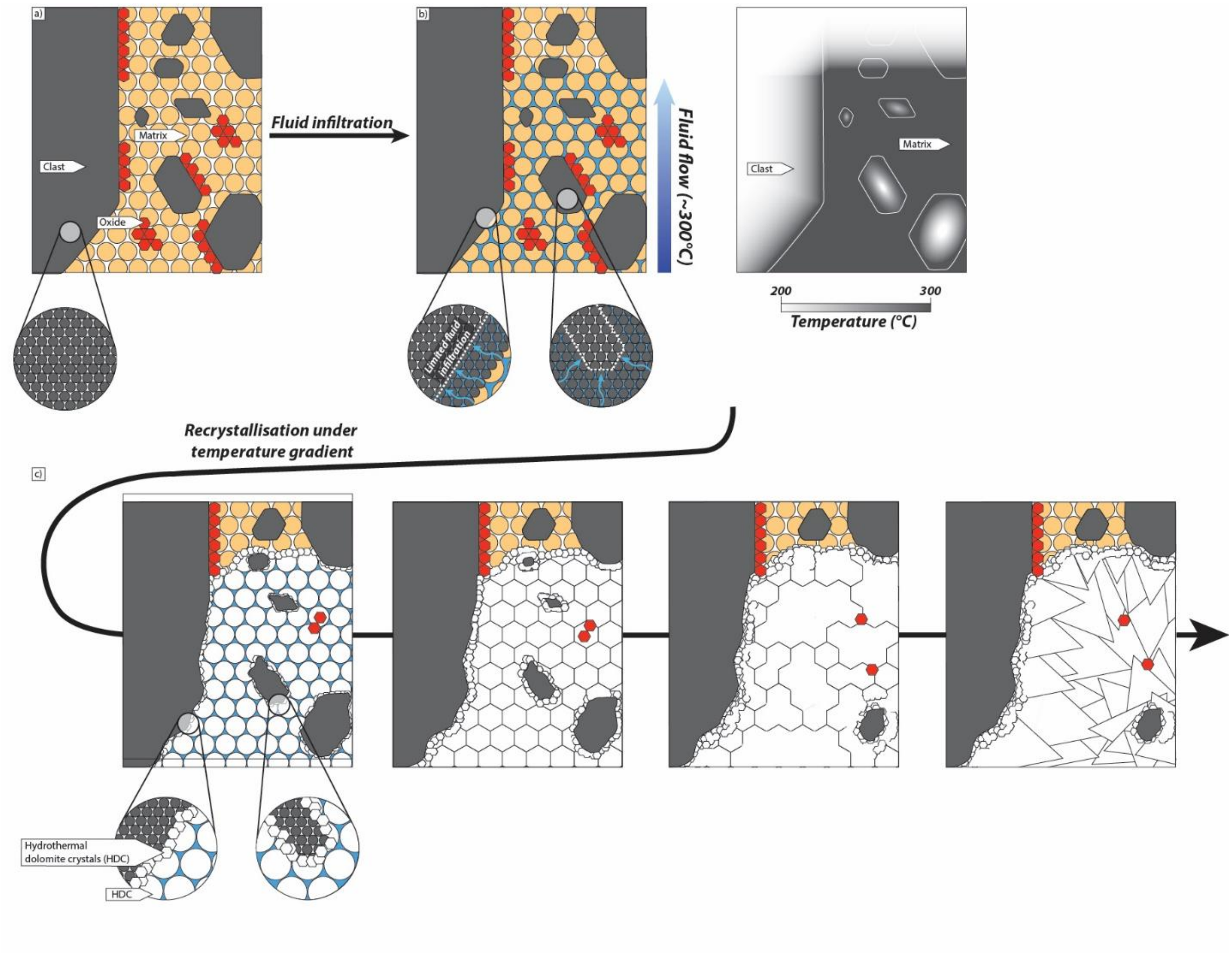

Fig. 10: Sketch illustrating a conceptual model leading to the complete replacement of the initial sedimentary breccia structure as coarse cement, mimicking the texture of hydrothermal dolomite breccia (as fluid overpressure). a) Original sedimentary breccia dolomite structure with oxides (red). b) Fluid infiltration through grain boundaries (blue) of a hot fluid (300°C) in the cold host rock (200°C). c) Step of recrystallization process triggered by temperature gradient, that pushes the oxides away. Reaction stops when the temperature gradient becomes too low.

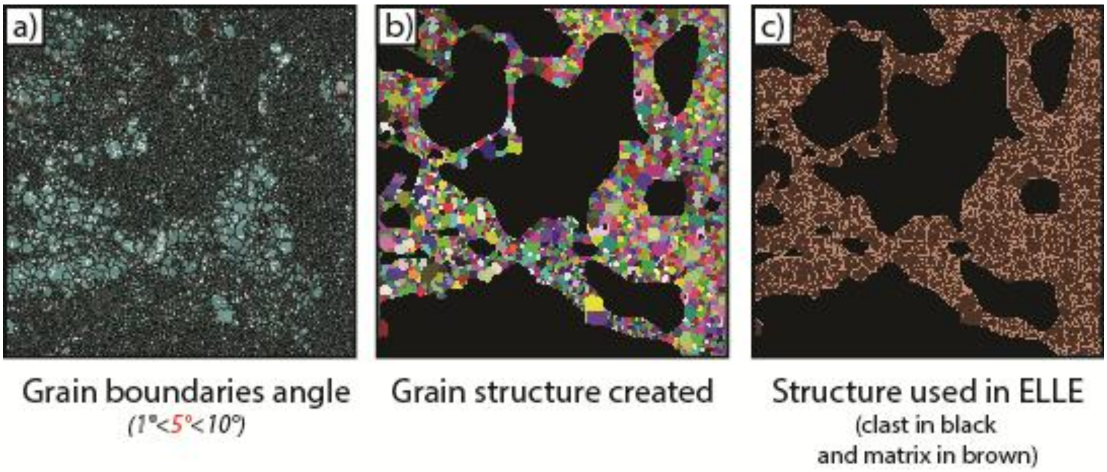

Fig. A1: Creation of a mesh usable for numerical simulation in the ELLE environment from the grain boundaries angles maps from EBSD (location Figure 6b). Black clasts are composed by small grain size less than 50 µm (circle equivalent diameter). For the simulation, the porosity of the grains is fixed to 4% based on BSE image analysis (Fig. 8). Right side has been changed to allow fluid to infiltrate rather than to be blocked by a clast.